Provable and Robust Wavefront Sensing via Self-Reference Interferometry

Nebiyou Yismaw[1], Vishwanath Saragadam[1], Aswin C. Sankaranarayanan[2], and M. Salman Asif[1] (✉)

[1] University of California, Riverside, CA, USA
{nyismaw, vishwans, sasif}@ucr.edu
[2] Carnegie Mellon University, Pittsburgh, PA, USA
saswin@andrew.cmu.edu

Abstract. Wavefront sensing involves estimating the phase and intensity of light, enabling a wide range of imaging applications, from adaptive optics and astronomy to biomedical imaging. Since conventional image sensors can only measure the spatial intensity distribution, phase retrieval arises as the central problem in wavefront sensing. Conventional interferometric approaches like phase-shifting interferometry (PSI) can recover phase information, but they rely on a stable reference beam that is difficult to realize in practical settings. To overcome this limitation, we propose a novel self-reference framework that relies on interference between shifted copies of the incoming wave; this results in pairwise phase differences between shifted pixels. We formulate an analytical solution for the complete phase retrieval based on the propagation of these differences across a connected graph. Furthermore, we provide a theoretical analysis of optimal measurement patterns, proving that co-prime shifts guarantee a connected graph and bound worst-case error accumulation, yielding a provably robust method. Extensive simulations demonstrate that complete phase profiles can be recovered from as few as eight shifted measurements, outperforming several existing approaches. Finally, we validate our framework using a hardware prototype, demonstrating real experiments for optical phase profile recovery, auto-refocusing, and imaging through scattering media.

1 Introduction

Light is an electromagnetic wave. While image sensors measure the spatial distribution of the intensity of this wave, a full description of the wave also involves its phase that is not directly measurable [8, 27]. Phase and intensity provide a complete description of the wave and enable capabilities including optical aberration correction [7, 28], quantitative phase imaging [32], imaging through scattering media [62], and digital holography [54].

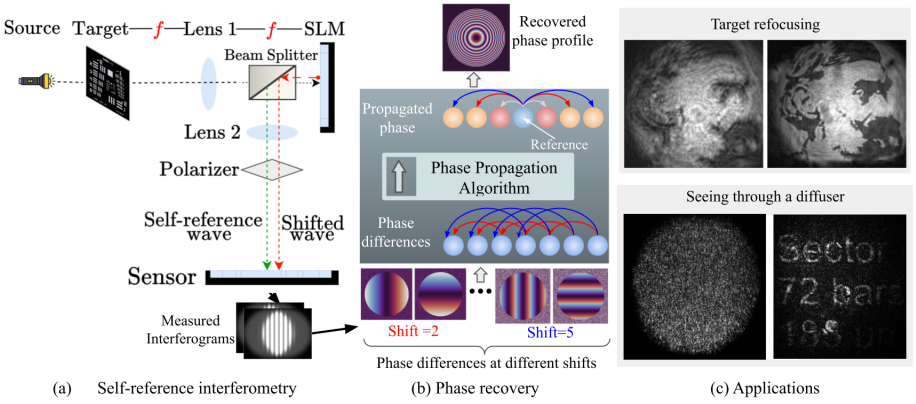

Fig. 1: Overview of the proposed wavefront sensing via self-reference interferometry. (a) Interference of the incoming wavefront with its spatially shifted copy (i.e. self reference) provides pairwise phase differences among shifted pixels. (b) Phase differences measured at multiple shifts are propagated using our proposed graph-based algorithm to recover the global phase profile. (c) The recovered phase enables applications such as target refocusing and imaging through a diffuser.

Phase retrieval from intensity-only measurements is a challenging and highly non-convex problem. The general phase retrieval problem can be defined as recovering a complex-valued signal $\boldsymbol{x}$ from its intensity measurements:

$$\boldsymbol{y} = |\mathcal{A}(\boldsymbol{x}) + \boldsymbol{r}|^2, \tag{1}$$

where $\mathcal{A}(\cdot)$ represents the imaging operator and $\boldsymbol{r}$ denotes a known or unknown reference. Structured Fourier transforms are the most common imaging operators in real-world optical systems [27] but geometric transforms and modulations are also feasible [10, 69]. In general, solving the phase retrieval problem requires nonlinear optimization, typically performed iteratively. Several classical [22, 24], model-based [11, 12], and deep learning-based [23, 34, 43] methods have been proposed for phase retrieval. **In this work, we seek to develop an analytical, non-iterative, and robust solution for phase retrieval.** Our method is non-iterative in the sense that the phase is recovered in a single phase propagation pass over image pixels rather than by repeatedly applying the forward and adjoint of the imaging operator $\mathcal{A}(\cdot)$ until convergence, as required by the optimization-based methods above. The phase propagation pass depends on connected pixels, which depends on the imaging operator design.

The choice of imaging operator or reference in Eq. (1) can simplify the phase retrieval problem. For instance, phase-shifting interferometry (PSI) [19, 30, 40] records interference of the unknown wave $\boldsymbol{x}$ with a known (phase-shifted) reference wave $\boldsymbol{r}$. The resulting phase retrieval solution can be written in an analytical form [3, 13, 42, 45]. PSI systems require a stable reference wave and protection against environmental perturbations, which makes the PSI setups bulky and difficult to realize in many real-world scenarios [20, 41, 67]. Self-reference PSI [49]

and common-path interferometry [60] mitigate these limitations by avoiding external reference waves and reducing environmental sensitivity. Our measurement design closely follows these strategies.

In this work, we present a simple, analytical, and provably robust method for self-reference PSI. Figure 1 illustrates our approach, where spatially shifted copies of the incoming wave interfere with each other, from which we extract pairwise phase differences that are integrated via a graph-based algorithm to recover the complete phase profile. We summarize our contributions as follows.

- **Self-referenced sensing model.** We introduce a self-referenced interferometric framework that uses spatially shifted copies of the incoming wave to extract pairwise phase differences between shifted pixels. The sensing model is physically realistic and enables a simple phase retrieval solution.
- **Robust and analytical phase retrieval algorithm.** We propose a simple, analytical, and robust solution that propagates pairwise phase differences across the measurement graph to recover the full phase profile. The method can be efficiently implemented using parallel propagation of multiple paths. A final refinement using least-squares offers improved recovery under noise, recovering complete phase profiles from as few as eight shifted measurements.
- **Optimal measurement design with provable guarantees.** The analytical solution for phase retrieval relies on the propagation of pairwise phase differences across a connected graph. We prove that co-prime shifts guarantee graph connectivity, and that the optimal co-prime pair minimizes the maximum hop length, which bounds worst-case error accumulation in our propagation algorithm.
- **Experimental validation and hardware prototype.** We validate the proposed framework through extensive simulations and a hardware prototype, demonstrating optical phase profile recovery, auto-refocusing, and imaging through scattering media.

2 Related Work

Wavefront sensing enables a broad range of applications, including adaptive optics [58] for astronomy [5, 16, 18, 51], optical metrology [68, 72], and biomedical imaging [6, 35, 46]. Existing methods broadly fall into interferometric and non-interferometric approaches.

2.1 Interferometry-based wavefront sensing

Phase-shifting interferometry. Interferometric methods recover the phase of an optical field by superimposing it with a reference beam or with a modified copy of itself and measuring the intensity patterns [9,15,29]. A widely used technique is *phase-shifting interferometry (PSI)* [19,30], where known phase shifts are introduced between a coherent reference beam and the unknown wavefront, and the resulting interference patterns are used to recover the phase. A key limitation

of PSI is that controlled phase shifting requires interferometric stability during acquisition, making it sensitive to vibration and turbulence [41]. Dynamic interferometry mitigates this issue by redesigning the acquisition process to reduce motion-induced phase errors [67]. Our method instead uses interference between shifted copies of the unknown wavefront to recover pairwise phase differences.

Common-path interferometry. To mitigate the sensitivity of PSI-based methods, *common-path interferometry* [25,60] ensures that the reference and unknown wavefronts share nearly identical optical paths, causing environmental perturbations to cancel as common-mode noise. The *point diffraction interferometer* [57] is an example of common-path interferometry in which a small pinhole spatially filters a portion of the unknown beam to generate a reference wave. Extensions of this idea include the *phase-shifting point diffraction interferometer* [42], using carefully-separated or learned references [33], and more recent reference-wave design approaches such as ReWave [13].

Lateral shearing interferometry. Another important class of common-path interferometric techniques is *lateral shearing interferometry* (LSI) [55,61], where the wavefront interferes with a laterally shifted copy of itself to encode phase differences between shifted points. Our measurement model is closely related, but we co-design the measurements and recovery by selecting co-prime shifts that connect every pixel to a reference through few propagation hops. This leads to an analytical propagation solution with reduced worst-case error accumulation.

2.2 Non-interferometric wavefront sensing

Slope-based wavefront sensors. A common class of non-interferometric wavefront sensors recover phase by measuring local wavefront slopes. Representative methods include the Shack–Hartmann sensor [47] and the pyramid wavefront sensor [48,63]. Such methods are limited by resolution and noise sensitivity [58].

Computational phase retrieval. Phase retrieval methods reconstruct the wavefront from intensity measurements at one or more planes, which is a challenging, highly nonlinear and nonconvex problem. Classical iterative methods such as Gerchberg-Saxton [24] alternate between spatial and Fourier domains, while later work spans coded diffraction patterns [10], convex relaxations such as PhaseLift [12], and nonconvex methods such as Wirtinger Flow [11] and alternating minimization [44]. Related techniques introduce measurement diversity, including ptychography and Fourier ptychography [52, 71] as well as diffraction tomography [65], but typically require scanning, multiple measurements, and iterative reconstruction.

Programmable optical modulation. Programmable optical modulation has been used to improve non-interferometric wavefront sensing [37, 69]. Several works use spatial light modulators (SLMs) to encode the incoming field with sequential phase patterns and recover the complex wavefronts from intensity-only measurements [21,39]. WISH [66] uses random phase modulation and alternating-projection phase retrieval [22] to reconstruct the field.

Deep learning-based phase retrieval. Supervised deep networks can be trained to predict phase from intensity [50,64], while model-based approaches use

learned denoisers within iterative schemes, including prDeep [43] with RED [53] and plug-and-play methods [34,36]. Untrained priors, such as Deep Image Prior (DIP) and Double-DIP, exploit convolutional architectures without external training [23,59]. Generative models and diffusion priors further regularize phase retrieval by enforcing consistency with intensity measurements [14,38,56], typically applying the prior to real-valued images.

3 Self Interference and Phase Propagation

Notations. We denote a complex wavefront as $\boldsymbol{x} = |\boldsymbol{x}|e^{j\boldsymbol{\phi}} = |\boldsymbol{x}| \odot \boldsymbol{p}$, where $\boldsymbol{\phi}$ is the phase map and $\boldsymbol{p} = e^{j\boldsymbol{\phi}}$ is the corresponding phasor map. Boldface denotes a full 2D array, and $\boldsymbol{x}(i)$, $\boldsymbol{p}(i)$, $\boldsymbol{\phi}(i)$ denote its value at pixel i. For a shift Δ_k, we define an operator $\mathcal{S}_{\Delta_k}(\cdot)$ that shifts an array by Δ_k pixels, so that $\mathcal{S}_{\Delta_k}(\boldsymbol{x})(i) = \boldsymbol{x}(i + \Delta_k)$. We use $\boldsymbol{p}_k$ to denote the phase-difference phasor map for shift Δ_k, where every ith entry encodes the phase difference between pixel i and $i + \Delta_k$: $\boldsymbol{p}_k(i) = e^{j(\boldsymbol{\phi}(i+\Delta_k)-\boldsymbol{\phi}(i))}$. $\boldsymbol{p}_k(i) = e^{j(\boldsymbol{\phi}(i+\Delta_k)-\boldsymbol{\phi}(i))}$. We use $\angle\boldsymbol{p}$ to represent the elementwise principal angle in $(-\pi, \pi]$.

3.1 Self interference and phase recovery

Suppose we represent the unknown complex-valued wave at some given plane as a 2D array $\boldsymbol{x} = |\boldsymbol{x}|e^{j\boldsymbol{\phi}} \equiv |\boldsymbol{x}| \odot \boldsymbol{p}$, where $\boldsymbol{\phi}$ denotes the phase, $\boldsymbol{p} = e^{j\boldsymbol{\phi}}$ denotes the phase component or unit phasor, and $\odot$ represents element-wise multiplication. **Self-reference interferometry** treats parts of the incident wave $\boldsymbol{x}$ as a reference (e.g., point diffraction interferometry [2,42,57]). We can use a single bright point in $\boldsymbol{x}$ as a reference (e.g., $\boldsymbol{x}(0)$) and capture measurements with multiple phase shifts, $\varphi_q \in \{0, \pi/2, \pi, 3\pi/2\}$, as

$$\boldsymbol{y}_q = |\boldsymbol{x} + \boldsymbol{x}(0)e^{j\varphi_q}|^2. \tag{2}$$

Since we can only recover the phase of $\boldsymbol{x}$ up to a global ambiguity, we select the phase of $\boldsymbol{x}(0)$ as a reference and set to zero (*i.e.* $\boldsymbol{x}(0) = |\boldsymbol{x}(0)|$, which is recovered directly from $\boldsymbol{y}_q(0)$). We can then recover the complete wave $\boldsymbol{x}$ as

$$\boldsymbol{y}_q = |\boldsymbol{x}|^2 + |\boldsymbol{x}(0)|^2 + 2\mathrm{Re}(\boldsymbol{x}|\boldsymbol{x}(0)|e^{-j\varphi_q}) \quad \Rightarrow \quad \boldsymbol{x} = \tfrac{1}{4|\boldsymbol{x}(0)|}\sum_q \boldsymbol{y}_q e^{j\varphi_q}. \tag{3}$$

A single point-based interference provides a closed-form solution for phase retrieval, but suffers from low signal-to-noise ratio. This is because the reference is typically created by passing the wave through a pinhole, which makes it very dim. The accuracy of phase-shifting interferometry improves with the brightness of the reference wave [4]. Recent methods such as ReWave [13] overcome this limitation by adaptively creating bright reference waves. In this paper, we seek to find similar simple solutions for different self-interferometric measurements.

Geometric transforms for self reference. Suppose we perform phase shifting interferometry by choosing a reference wave that is a translated copy of the

incident wave $\boldsymbol{x}$. We can represent such shifted interferometric measurements as

$$\begin{aligned}\boldsymbol{y}_{k,q} &= |\boldsymbol{x} + e^{j\varphi_q}\mathcal{S}_{\Delta_k}(\boldsymbol{x})|^2 + \boldsymbol{\eta}_{k,q} \\ &\equiv |\boldsymbol{x}|^2 + |\mathcal{S}_{\Delta_k}(\boldsymbol{x})|^2 + 2\mathrm{Re}\left(|\boldsymbol{x}| \odot |\mathcal{S}_{\Delta_k}(\boldsymbol{x}^*)| e^{j(\boldsymbol{\phi} - \mathcal{S}_{\Delta_k}(\boldsymbol{\phi}) - \varphi_q)}\right) + \boldsymbol{\eta}_{k,q},\end{aligned} \tag{4}$$

where Δ_k encodes the 2D shift vector, $\mathcal{S}_{\Delta_k}(\cdot)$ represents an operator that shifts input by Δ_k pixels, $\varphi_q = \frac{\pi}{2}q$ represents the quadrature phases with $q \in \{0, 1, 2, 3\}$, and $\boldsymbol{\eta}_{k,q}$ represents the measurement noise. We can potentially capture such PSI measurements for K such translations so that $k \in \{1, \ldots, K\}$. While the system in Eq. (4) does not provide a closed-form solution like the one in Eq. (3), we can recover the wave using a simple (graph propagation-based) solution.

Phase difference propagation. Our key observation is that we can compute the pairwise phase differences from the measurements in Eq. (4), which can then be combined to recover the complete phase profile. In particular, we estimate the following phasors from the noisy quadrature measurements:

$$\begin{aligned}\sum_q \boldsymbol{y}_{k,q} e^{-j\varphi_q} &\approx 4|\boldsymbol{x}| \odot |\mathcal{S}_{\Delta_k}(\boldsymbol{x})| e^{j(\mathcal{S}_{\Delta_k}(\boldsymbol{\phi}) - \boldsymbol{\phi})} \\ \Rightarrow \boldsymbol{p}_k &= \frac{\sum_q \boldsymbol{y}_{k,q} e^{-j\varphi_q}}{|\sum_q \boldsymbol{y}_{k,q} e^{-j\varphi_q}|} \approx e^{j(\mathcal{S}_{\Delta_k}(\boldsymbol{\phi}) - \boldsymbol{\phi})},\end{aligned} \tag{5}$$

where the approximations arise from measurement noise. In other words, we can estimate unit phasors $\boldsymbol{p}_k$ that encode phase differences between all pixels shifted by Δ_k. We can assume one pixel as a reference with zero phase (e.g., $\boldsymbol{\phi}(0) = 0, \boldsymbol{p}(0) = 1$), and compute the relative phase at any other pixel that is connected to the reference pixel by propagating the phasors in Eq. (5) to the reference. **For robust and complete phase recovery, we need measurements that yield a graph with every pixel connected to the reference pixel with minimal path length.**

Connection to phase unwrapping. Our formulation is loosely connected to phase unwrapping [26,31], which removes 2π ambiguities from a known wrapped phase map. These methods assume that the wrapped phase is available, whereas our method recovers the phase directly from intensity measurements. A connection nonetheless arises, as the estimated pairwise phase differences would be wrapped, and our graph propagation in the phasor form integrates the phase differences along a connected path while resolving the phase ambiguities.

3.2 Single shift and single-path propagation

Let us first consider measurements with a single-pixel shift, as illustrated in Fig. 2(a) for a single row. Suppose we record $\boldsymbol{y}_{1,q}$ with $\Delta_1 = (1, 0)$ as a single-pixel horizontal shift. We can calculate the phasors for the phase differences between adjacent pixels using Eq. (5) as $\boldsymbol{p}_1$. We can then start with the reference pixel phase ($\boldsymbol{p}(0) = 1$) and estimate phasors for all the connected pixels as $\widehat{\boldsymbol{p}}(1) =$

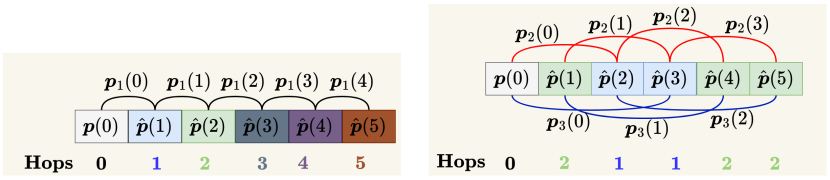

(a) Single shift (b) Two Shifts (2,3)

Fig. 2: Comparison of phasor propagations by single- and two-shift measurements for $N = 9$. Note that $\boldsymbol{p}(i) = e^{j\boldsymbol{\phi}(i)}$ denotes the unit phasor of original phase at node i, whereas $\boldsymbol{p}_k(i)$ denotes the unit phasor that encodes phase difference between node i and $i + \Delta_k$. (a) A single shift ($\Delta_1 = 1$) forms a path graph with linearly increasing hop distance from the reference. (b) Two shifts ($\Delta_2 = 2$, $\Delta_3 = 3$) introduce long-range connections that reduce the maximum hop count and shorten propagation paths.

$\boldsymbol{p}_1(0)$, $\widehat{\boldsymbol{p}}(2) = \widehat{\boldsymbol{p}}(1)\boldsymbol{p}_1(1)$, and $\widehat{\boldsymbol{p}}(i+1) = \widehat{\boldsymbol{p}}(i)\boldsymbol{p}_1(i)$ for any i. In other words, we can propagate the phasors to all the connected pixels as $\widehat{\boldsymbol{p}}(i + \Delta_1) = \widehat{\boldsymbol{p}}(i)\boldsymbol{p}_1(i)$.

A single pixel shift in the horizontal and vertical directions would provide a connected graph for a 2D array. In principle, we can propagate the phasors for phase differences and estimate the complete phase profile. In practice, the phase differences will be estimated from noisy measurements, which will lead to noisy estimates. The single-pixel shift-based measurements under noisy conditions are prone to error accumulation (as shown in Fig. 3). Let us assume that each phase difference estimation incurs an independent error ϵ with zero mean and variance σ^2. In the case of single-pixel shifts, the error accumulation at any pixel will be proportional to its distance from the reference pixel.

3.3 Two shifts and multi-path propagation

Multiple shifts can provide multiple propagation paths and reduce effective path lengths and error accumulation in the phasor propagation. Let us consider two distinct shifts Δ_s, Δ_t and the corresponding (estimated) phase-difference phasors $\boldsymbol{p}_s, \boldsymbol{p}_t$. For instance, in Fig. 2(b), we choose $\Delta_s = 2, \Delta_t = 3$ and compute $\boldsymbol{p}_2, \boldsymbol{p}_3$. Assuming $\boldsymbol{p}(0) = 1$, we can estimate the phasors at node 2,3 that are directly connected to 0 as $\widehat{\boldsymbol{p}}(2) = \boldsymbol{p}_2(0), \widehat{\boldsymbol{p}}(3) = \boldsymbol{p}_3(0)$. We can then propagate these phasors to estimate $\widehat{\boldsymbol{p}}(4) = \widehat{\boldsymbol{p}}(2)\boldsymbol{p}_2(2), \widehat{\boldsymbol{p}}(5) = \widehat{\boldsymbol{p}}(2)\boldsymbol{p}_3(2), \widehat{\boldsymbol{p}}(1) = \widehat{\boldsymbol{p}}(3)\boldsymbol{p}_2^*(1)$. Note that to estimate phasor at node 1, we use the estimate at node 3 and then the phasor of difference from 3 to 1. The maximum path length (or hop distance) reduces to 2, which is a significant improvement over the maximum path length of 4 in the single-shift case.

We can reduce the path length of phasor propagation by carefully selecting the shifts Δ_s and Δ_t as multiple shifts introduce new connections between the reference pixel and the rest of the graph. These connections allow information to propagate in larger steps and fewer hops compared to the single-shift case. The next logical question is how to choose Δ_s and Δ_t to ensure complete and robust propagation. We discuss this in Sec. 4, where we prove that co-prime shifts guarantee full connectivity and minimum path length.

Algorithm 1 Phase Retrieval for Self-Reference Interferometry

Require: Phase-difference phasors $\{\boldsymbol{p}_k\}_{k=1}^K$, shifts $\{\Delta_k\}_{k=1}^K$, reference node i_0
Initialize phasor estimate $\widehat{\boldsymbol{p}}$ with reference node $\widehat{\boldsymbol{p}}(i_0) = 1$
Initialize queue $\mathcal{Q} \leftarrow \{i_0\}$
Initialize hops $h(i) \leftarrow \infty \, \forall i \neq i_0$; set $h(i_0) \leftarrow 0$ ▷ *Track hop length from the reference*
while $\mathcal{Q} \neq \emptyset$ **do**
    Pop $i \leftarrow$ dequeue($\mathcal{Q}$)
    for each neighbor i' reachable via any shift in $\{\Delta_k\}$ **do**
        $\boldsymbol{p}' \leftarrow \widehat{\boldsymbol{p}}(i) \cdot \boldsymbol{p}_k(i)$ ▷ *Apply phasor difference*
        if $h(i') = \infty$ **then** ▷ *Node has not been visited*
            Set phase: $\widehat{\boldsymbol{p}}(i') \leftarrow \boldsymbol{p}'$
            Set $h(i') \leftarrow h(i) + 1$ ▷ *Increment hop length*
            Enqueue (i') ▷ *Push node to queue*
        else if $h(i') = h(i) + 1$ **then** ▷ *Node was visited with the same hop length*
            $\widehat{\boldsymbol{p}}(i') \leftarrow \text{avg}(\widehat{\boldsymbol{p}}(i'), \boldsymbol{p}')$ ▷ *Average equal hop phasors*
        end if ▷ *Discard any phasors with longer hop length*
    end for
end while
return phase $\widehat{\boldsymbol{\phi}} = \angle \widehat{\boldsymbol{p}}$ ▷ *Compute phases from phasors*

3.4 Multiple shifts and multi-path propagation

The general phase recovery process with K shifts $\{\Delta_k\}_{k=1}^K$ can be formulated as the propagation of phase-difference phasors $\{\boldsymbol{p}_k\}_{k=1}^K$ over a graph whose vertices correspond to pixels and whose edges correspond to the estimated phase-difference phasors, as shown in Fig. 2 for 1 or 2 shifts. For complete connectivity, the shifts must be co-prime (see Sec. 4.1).

A general algorithm for our method is presented in Algorithm 1. The method takes $\{\Delta_k\}$, $\{\boldsymbol{p}_k\}$, and a reference pixel as input. The algorithm maintains a queue of nodes $\mathcal{Q}$, which operates in a breadth-first search manner and provides starting nodes for phase propagation at each iteration. The queue is initialized with the reference node. In the first iteration, the phasors of the neighbors reachable from the reference through each shift are computed as $\widehat{\boldsymbol{p}}(\Delta_k) = \boldsymbol{p}(0)\,\boldsymbol{p}_k(\Delta_k)$ and added to the queue. The algorithm then iteratively dequeues elements and propagates phasors from each node to its neighbors. To ensure consistency, a node is only updated if it has not been visited before. Additionally, to improve robustness, propagated phasors from multiple paths are averaged when the paths have the same distance from the reference node.

Efficient parallel implementation. The proposed method shown in Algorithm 1 processes one pixel at a time, which is inherently sequential. For parallel GPU implementation, we reformulate the propagation as an iterative wavefront expansion, where at every iteration, all the visited pixels simultaneously propagate their phase estimates to all valid neighbors via vectorized tensor operations. We present details of the implementation in the supplementary material.

Noise reduction via hop-constrained path averaging. We can reduce the variance in the phase estimate by averaging multiple non-redundant propagation

paths that reach the same node/pixel. Since the estimation error accumulates with path length (see Sec. 3.2), we restrict averaging to paths with equal hop lengths and discard paths with larger hop lengths (as they potentially represent larger accumulated noise). This hop-constrained averaging reduces variance without introducing additional bias. This strategy allows us to introduce an additional design axis for propagation.

Global least-squares refinement. We can further refine $\widehat{\boldsymbol{\phi}}$, estimated using multi-shift propagation (Algorithm 1), by jointly fitting it to all the measured phase differences via a global least-squares step. Let $\nabla_k \boldsymbol{\phi} = \angle \boldsymbol{p}_k$ denote the wrapped phase differences estimated in Eq. (4) and $\mathcal{D}_{\Delta_k} = \mathcal{S}_{\Delta_k} - I$ denote the forward-difference operator for shift Δ_k. The phase differences are obtained from the estimated phasors $\boldsymbol{p}_k$, which lie on the unit circle, so $\nabla_k \boldsymbol{\phi} = \angle \boldsymbol{p}_k \in (-\pi, \pi]$ recovers the true difference $\mathcal{D}_{\Delta_k} \boldsymbol{\phi}$ only modulo 2π. We first estimate the integer offsets as $m_k = \text{round}\left(\left(\mathcal{D}_{\Delta_k} \widehat{\boldsymbol{\phi}} - \nabla_k \boldsymbol{\phi}\right)/2\pi\right)$, and unwrap the phase difference measurements as $\nabla_k \boldsymbol{\phi}^{\text{unwrap}} = \nabla_k \boldsymbol{\phi} + 2\pi m_k$. The refined phase can then be obtained by solving $\min_{\boldsymbol{\phi}} \sum_{k=1}^{K} \|\mathcal{D}_{\Delta_k} \boldsymbol{\phi} - \nabla_k \boldsymbol{\phi}^{\text{unwrap}}\|_2^2$. Since $\mathcal{D}_{\Delta_k}$ is a difference operator, it can be viewed as a convolution of $\boldsymbol{\phi}$ with a filter $\boldsymbol{d}_{\Delta_k}$, which can be diagonalized in the Fourier domain. The least-squares solution thus has a simple closed-form expression in the Fourier domain:

$$\widehat{\boldsymbol{\phi}}_{LS} = \mathcal{F}^* \left(\frac{\sum_k (\overline{\mathcal{F}(\boldsymbol{d}_{\Delta_k})} \odot \mathcal{F}(\nabla_k \boldsymbol{\phi}^{\text{unwrap}}))}{\sum_k |\mathcal{F}(\boldsymbol{d}_{\Delta_k})|^2 + \lambda} \right), \tag{6}$$

where $\mathcal{F}$ is the Fourier transform operator, division and multiplications are element-wise, and λ is a regularizer.

4 Provable and Optimal Sensing with Co-Prime Shifts

A complete and stable phase recovery depends on the graph connectivity and maximum path length with respect to the reference node. The choice of shifts $\{\Delta_k\}$ determines the graph connections and these properties. We seek to select $\{\Delta_k\}$ that guarantee **full connectivity** such that every pixel is connected to the reference node through some path and limit the **maximum path length** that in turn limits the worst-case hop distance and the associated error accumulation. In this section, we show that co-prime shifts guarantee full connectivity and minimum path length.

We model the phase recovery problem as propagation over a graph of pixels, as illustrated in Fig. 2. For simplicity, let us assume the graph consists of N pixels/nodes that are indexed as

$$V = \left\{ -\left\lfloor \tfrac{N}{2} \right\rfloor, \ldots, \left\lfloor \tfrac{N}{2} \right\rfloor - 1 \right\}. \tag{7}$$

An *edge* exists between node i and j if we have direct phase difference measurements between them as $\nabla_k \boldsymbol{\phi}$. For a set of shifts $\mathcal{S} = \{s_1, s_2, \ldots, s_K\}$, the edge set is

$$E(\mathcal{S}) = \left\{ (i, i + s_k) : i, i + s_k \in V,\ s_k \in \mathcal{S} \right\}. \tag{8}$$

Phase propagation can then be viewed as a traversal along this graph. Starting from a reference node, which is assumed to have known or zero phase, we integrate along edges to estimate phases at all other nodes. The *hop distance* between two nodes is defined as the minimum number of edges that must be traversed to connect them. The *diameter* of the graph, which is the maximum hop distance from the reference node to any other node, directly determines the worst-case accumulation of measurement noise.

4.1 Connectivity guarantees

We now formalize the conditions under which a graph defined by two shifts of size s and t is guaranteed to be fully connected. In Theorem 1, we establish that if the shifts s and t are co-prime, meaning that their greatest common divisor satisfies $\gcd(s,t) = 1$, and if $s + t \leq N$, then every node in V is reachable from the reference node 0 via a sequence of hops along edges. This result relies on two key observations: Lemma 1 shows that by taking repeated steps of size s, we can generate all residues of $\mod (s+t)$, and Lemma 2 shows that there is a sliding window of locally connected nodes that connects every node to the reference. The complete proofs of these lemmas and Theorem 1 are provided in the supplementary material.

Lemma 1 (Co-prime residue coverage). *Let $k \geq 1$, $s \in \mathbb{Z}$ and $\gcd(s,k) = 1$. Then for any $p \in \mathbb{Z}$,*

$$\{(p + is) \bmod k \ : \ i = 0, 1, \ldots, k-1\} = \{0, 1, \ldots, k-1\}.$$

Lemma 2 (Sliding window coverage). *Let $s, t \in \mathbb{N}$ with $s + t \leq N$, and let V be defined as Eq. (7). For any $x \in V$, there exists an interval I_1 of size $s + t$ containing x, and a finite sequence of intervals $I_1, I_2, \ldots, I_K$ (for some $K \in \mathbb{N}$) of size $s + t$, each contained in V, such that consecutive intervals share at least one common element and I_K contains 0.*

Theorem 1 (Connectivity via co-prime shifts). *Let $s, t \in \mathbb{N}$ be co-prime (*i.e. $\gcd(s,t) = 1$*), the graph V as defined in Eq. (7), and edges $E(\{s,t\})$ as defined in Eq. (8) using shifts s and t. Then every node in V is reachable from the reference node through a sequence of hops along edges, provided $s + t \leq N$.*

4.2 Optimal co-prime shift design

With connectivity established, we now determine shift pairs that minimize the maximum hop distance. Lemma 3 establishes a universal lower bound on the maximum hop distance and Theorem 2 shows that co-prime shifts near $\sqrt{N/2}$ achieve this bound.

Lemma 3 (Lower bound on maximum hop distance). *Consider the graph V with N nodes defined in Eq. (7) and edges $E(\{s,t\})$ as in Eq. (8). Let $h^\star$ denote the minimum number of hops required to reach all nodes from a reference node. Then, for any choice of two shifts, $h^\star \geq \left\lceil \frac{-1+\sqrt{2N-1}}{2} \right\rceil$.*

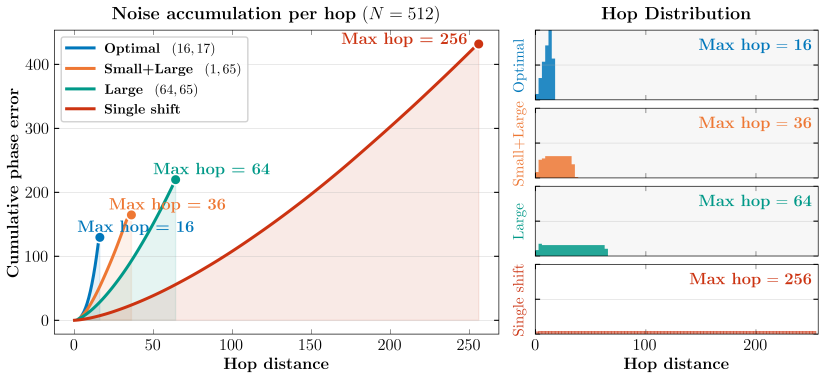

Fig. 3: Cumulative absolute phase error (radians) vs. hop length for $N = 512$ (left) and hop-length histograms (right). Given a fixed error budget, the optimal co-prime pair $(16, 17)$ minimizes the maximum hop length. Other shift choices require larger maximum hops.

Theorem 2 (Optimal shift pair). *For a graph with N nodes as in Eq. (7) and edges defined by the consecutive* ***co-prime*** *pair $s, t \in \mathbb{N}$, $s = \left\lfloor \sqrt{\frac{N}{2}} \right\rfloor$ and $t = \left\lfloor \sqrt{\frac{N}{2}} \right\rfloor + 1$, achieves the minimum possible hop distance $h^\star$ given in Lemma 3.*

4.3 Noise analysis and optimality

We conduct simulations to validate our analysis that reconstruction error increases with hop length and that optimal shifts Theorem 2 minimize error accumulation. We generate noisy phase differences Eq. (5) by adding Gaussian noise to ground-truth phases and recover the phase using Algorithm 1.

As shown in the left panel of Fig. 3 for $N = 512$, the cumulative phase error increases monotonically with hop distance, confirming that longer propagation paths accumulate more noise. Given a fixed error budget, the optimal shifts $s = \lfloor \sqrt{N/2} \rfloor = 16$ and $t = s + 1 = 17$ minimize the maximum hop distance $h^\star = 16$. The right panel of Fig. 3 further shows that the hops for our optimal shifts are tightly concentrated, while other choices produce larger maximum hops. By bounding the maximum hop distance, our design caps the worst-case per-pixel error, while the concentrated hop distribution keeps the total accumulated error low. Additional supporting results are in the supplementary material.

5 Experiments

5.1 Simulation experiments

We evaluate phase recovery from shifted interferometric measurements in a synthetic setting and compare reconstruction accuracy with related baseline methods. To generate simulated data, we use 100 images from the DIV2K validation

Table 1: Phase errors (mean ± std) at 22 dB SNR. Our method achieves the best or second-best results across all phase profiles. (Best bold, second-best underlined).

Method \ #Meas.	Quadratic phase		Random phase		Smooth phase (peaks)	
	16	32	16	32	16	32
GD-Rand	0.695 ± 0.365	0.470 ± 0.434	**0.138 ± 0.148**	**0.079 ± 0.152**	0.791 ± 0.361	0.570 ± 0.404
GD-Spec	0.737 ± 0.400	0.400 ± 0.432	0.691 ± 0.367	0.449 ± 0.440	0.686 ± 0.397	0.371 ± 0.374
WISH	0.852 ± 0.299	0.423 ± 0.366	0.854 ± 0.320	0.453 ± 0.377	0.898 ± 0.330	0.425 ± 0.367
PnP-FISTA	0.669 ± 0.341	0.456 ± 0.304	0.735 ± 0.329	0.425 ± 0.264	0.663 ± 0.341	0.479 ± 0.338
DIP	1.486 ± 0.031	1.491 ± 0.051	1.495 ± 0.037	1.447 ± 0.065	1.442 ± 0.063	1.423 ± 0.081
Ours	**0.158 ± 0.104**	**0.099 ± 0.083**	0.156 ± 0.099	0.094 ± 0.075	**0.155 ± 0.096**	**0.097 ± 0.071**
Ours with LS	0.183 ± 0.082	0.126 ± 0.065	0.158 ± 0.075	0.121 ± 0.055	0.205 ± 0.063	0.159 ± 0.050

dataset [1] as ground truth intensity patterns. For each image, we synthesize complex wavefronts by combining the intensity with three types of phase profiles: random, quadratic, and smooth profiles[3]. We simulate interferometric measurements using Eq. (4) with Poisson and Gaussian noise at multiple SNRs and shifts. We used the optimal shifts $\Delta_1 = 16$ and $\Delta_2 = 17$ for the 16-measurement setup (*i.e.* 2 shifts × 2 directions (H, W) × 4 quadratures), and included $\Delta_3 = 23$ and $\Delta_4 = 31$ for the 32-measurement experiments.

We compare against gradient descent–based phase retrieval with random initialization (**GD-Rand**) and spectral initialization [44] (**GD-Spec**), a plug-and-play recovery method (**PnP-FISTA**) [36] that uses a pretrained **DRUNet** denoiser [70] as a denoiser prior, the wavefront sensing method **WISH** [66] that uses Gerchberg–Saxton iterations [22,24], and a Deep Image Prior (**DIP**)–based approach [59] using a convolutional decoder architecture from [17] as a phase prior. Although the original WISH uses random phase modulation, we replace it with phase ramps to generate shifted measurements in our setup. Additional details are provided in the supplementary material.

We evaluate phase recovery using the mean absolute phase error after global phase correction. Given estimated phasors $\widehat{\boldsymbol{p}}$ and ground-truth phasors $\boldsymbol{p}_{gt}$, we estimate the global phase offset θ from the circular mean of their phase differences and measure the residual error as $\mathcal{E}_{\text{phase}} = \frac{1}{N}\sum_{i=1}^{N}\left|\angle\big(\widehat{\boldsymbol{p}}(i)\boldsymbol{p}_{gt}^{*}(i)e^{-j\theta}\big)\right|$. We report the mean phase error (± standard deviation) at SNR ≈ 22 dB in Tab. 1, where our method achieves the lowest error for both quadratic and smooth phase profiles. As shown in Fig. 4, with 16 measurements it is the only approach that reconstructs a phase profile consistent with the ground truth. For random phase, gradient descent with random initialization yields a lower error (see Fig. 4). The performance gap is small and disappears at higher SNR, as shown in Fig. 5. Figure 5 further shows that least-squares refinement (**Ours + LS**) yields clear improvements under noisy measurements. Additional results under varying noise and measurement settings are provided in the supplementary material.

Computation time. We compare runtime per reconstruction across methods on a single NVIDIA RTX 6000 Ada GPU. Our approach is the fastest at 1.2s,

[3] The MATLAB `peaks` function is used to generate smooth synthetic profiles.

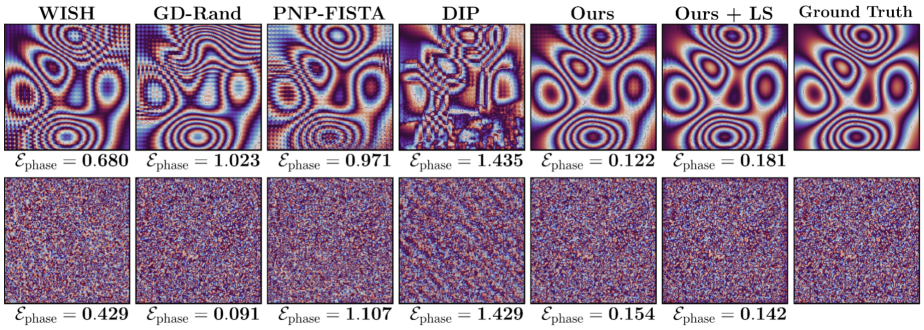

Fig. 4: Phase recovery of smooth and random phase profiles (SNR 22 dB, 16 measurements). Our method achieves the lowest error on smooth profiles and remains competitive for random phases.

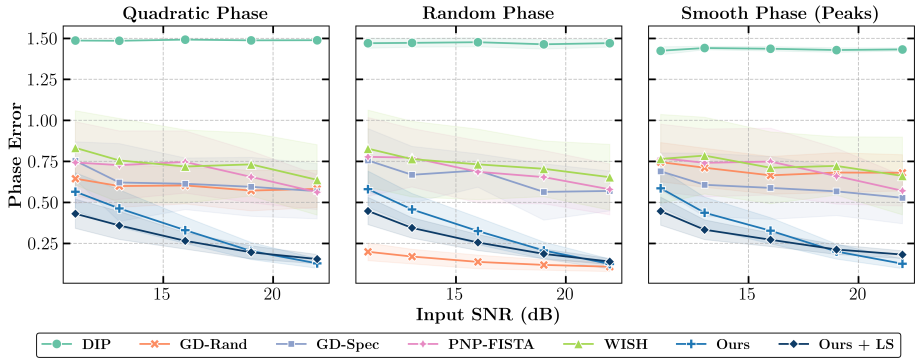

Fig. 5: Phase recovery performance across SNRs in simulations. Our method demonstrates consistent performance across all phase types, maintaining the lowest error in most settings and highly competitive results otherwise. Notably, least-squares refinement (*Ours + LS*) significantly improves reconstruction accuracy at low SNRs.

compared to 1.5s for gradient-based optimization, 3.6s for WISH, 8.7s for DIP, and 10.7s for PnP-FISTA. Overall, this corresponds to an approximately 8× reduction in computation time relative to the slowest baseline.

5.2 Hardware prototype

We implement a hardware prototype shown in Fig. 6, following the optical layout in Fig. 1, to further validate the proposed self-referenced PSI framework. A $4f$ optical system with a phase-only SLM at the Fourier plane generates spatial shifts via phase ramps. This setup allows us to record both interference patterns for

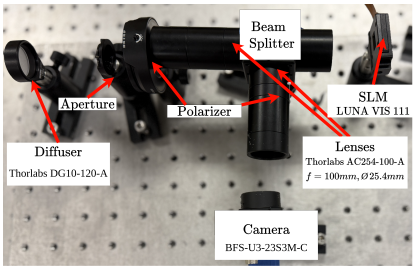

Fig. 6: Hardware prototype.

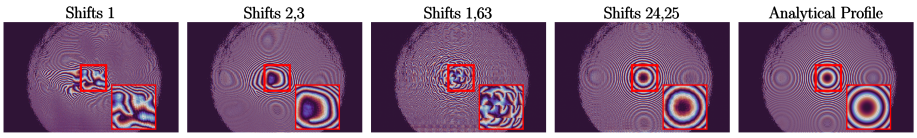

Fig. 7: Optical phase recovery of a biconvex lens ($f = 75$ mm). Recovered phase under different shifts; the last column is the analytical thin-lens reference. Optimal co-prime shifts $(24, 25)$ closely match the analytical rings (visible in the zoomed views), while non-optimal shifts introduce discontinuities and artifacts.

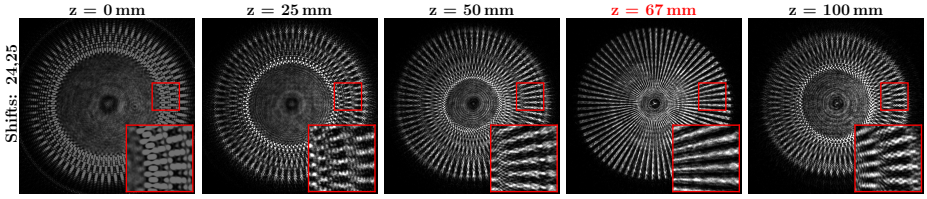

Fig. 8: Target refocusing. We recover an out-of-focus complex field and numerically propagate it to multiple distances. Optimal focus is achieved at $z = 67$ mm, where the star pattern and fine features are clearly resolved.

phase retrieval and unmodulated captures of the scene to directly measure the amplitude. Additional hardware implementation details are provided in the supplementary material.

Optical phase recovery. We place objects in the input plane and recover their phase profile. Figure 7 shows the recovered phase profile of a biconvex lens of focal length $f = 75$ mm under different shifts, with the analytical thin-lens phase shown in the last column. For visualization, the phase is masked by the measured amplitude. We observe that the optimal shift pair $(24, 25)$ produces the most accurate and stable reconstructions, closely matching the analytical profile. Other shift pairs, as shown in Fig. 7, lead to suboptimal phase estimates. Additional results on biconvex lenses are provided in the supplementary material.

Target refocusing. We place a target away from the input plane and capture it out-of-focus. Our algorithm recovers the complex field at the input plane, whose amplitude remains blurred (first column of Fig. 8). Applying Fresnel propagation [27] to the recovered wavefront, the target progressively refocuses with increasing propagation distance, yielding a sharp image at the correct depth (last column of Fig. 8). This confirms the recovered phase is physically consistent and preserves the correct wavefront profile required for accurate refocusing. Additional refocusing examples are provided in the supplementary material.

Seeing through a diffuser. We place a thin diffuser (DG10-120-A, Thorlabs) in front of the target, which scatters the wavefront and produces a speckle-like pattern (first column of Fig. 9). Our method reconstructs the complex field at the input plane (second column), which is then numerically propagated to the diffuser plane. There, we undo the effects of the diffuser by multiplying with the conjugate of the calibrated diffuser phase profile. The phase maps after correction

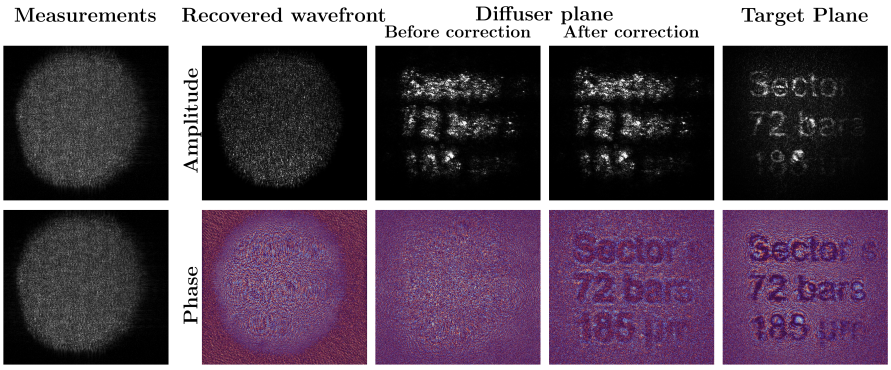

Fig. 9: Seeing through a diffuser. We recover the scattered complex field and computationally propagate it to the diffuser plane for phase correction. Subsequent propagation to the object plane successfully reveals the target, which is otherwise invisible.

(third column of Fig. 9) show the structure of the target and propagating the corrected field to the target plane reveals the object's amplitude and phase.

6 Conclusion

We present a principled framework for wavefront phase recovery from shifted self-interference measurements. Our method gives a simple analytical solution by propagating phase differences on a connected graph, where the choice of shifts controls graph structure and error accumulation. We prove that co-prime shift pairs guarantee full connectivity and yield a provably optimal design that minimizes hop length and worst-case error. Simulations confirm that our optimal shifts consistently outperform existing methods, and hardware experiments validate the approach in practice. Together, these establish an accurate and robust wavefront sensing method.

Limitations and Future Work. Our method currently averages equal-hop paths uniformly. Weighted combination by reliability, as in quality-guided phase unwrapping [31], could improve robustness, particularly for random phase profiles where we empirically observe suboptimal performance. Our prototype captures phase-shifted measurements sequentially with an SLM, assuming a nearly static field and extending it to dynamic adaptive optics is a promising direction.

Acknowledgements

This work is partially supported by the NSF awards CCF-2046293 and CCF-2504614.

References

1. Agustsson, E., Timofte, R.: NTIRE 2017 challenge on single image super-resolution: Dataset and study. In: IEEE Conf. Comput. Vis. Pattern Recog. Worksh. (2017)
2. Akondi, V., Jewel, A., Vohnsen, B.: Digital phase-shifting point diffraction interferometer. Optics Letters **39**(6), 1641–1644 (2014)
3. Andersen, G.P., Dussan, L., Ghebremichael, F., Chen, K.: Holographic wavefront sensor. Optical Engineering **48**(8), 085801–085801 (2009)
4. Anderson, C.S.: Fringe visibility, irradiance, and accuracy in common path interferometers for visualization of phase disturbances. Applied Optics **34**(32), 7474–7485 (1995)
5. Beckers, J.M.: Adaptive optics for astronomy: Principles, performance, and applications. Annual Review of Astronomy and Astrophysics **31**, 13–62 (1993)
6. Booth, M.J.: Adaptive optics in microscopy. Philosophical Transactions of the Royal Society A: Mathematical, Physical and Engineering Sciences **365**(1861), 2829–2843 (2007)
7. Booth, M.J.: Adaptive optical microscopy: the ongoing quest for a perfect image. Light: Science & Applications **3**(4), e165–e165 (2014)
8. Born, M., Wolf, E.: Principles of optics: electromagnetic theory of propagation, interference and diffraction of light. Elsevier (2013)
9. Bruning, J.H., Herriott, D.R., Gallagher, J.E., Rosenfeld, D.P., White, A.D., Brangaccio, D.J.: Digital wavefront measuring interferometer for testing optical surfaces and lenses. Applied Optics **13**(11), 2693–2703 (1974)
10. Candes, E.J., Li, X., Soltanolkotabi, M.: Phase retrieval from coded diffraction patterns. Applied and Computational Harmonic Analysis **39**(2), 277–299 (2015)
11. Candes, E.J., Li, X., Soltanolkotabi, M.: Phase retrieval via Wirtinger flow: Theory and algorithms. IEEE Transactions on Information Theory **61**(4), 1985–2007 (2015)
12. Candes, E.J., Strohmer, T., Voroninski, V.: PhaseLift: Exact and stable signal recovery from magnitude measurements via convex programming. Communications on Pure and Applied Mathematics **66**(8), 1241–1274 (2013)
13. Chen, W.Y., Levin, A., O'Toole, M., Sankaranarayanan, A.C.: Reference wave design for wavefront sensing. In: 2021 IEEE International Conference on Computational Photography (ICCP) (2021)
14. Chung, H., Kim, J., Mccann, M.T., Klasky, M.L., Ye, J.C.: Diffusion posterior sampling for general noisy inverse problems. arXiv preprint arXiv:2209.14687 (2022)
15. Creath, K.: V phase-measurement interferometry techniques. In: Progress in Optics, vol. 26, pp. 349–393. Elsevier (1988)
16. van Dam, M.A., Bouchez, A.H., Le Mignant, D., Johansson, E.M., Wizinowich, P.L., Campbell, R.D., Chin, J.C., Hartman, S.K., Lafon, R.E., Stomski Jr, P.J., et al.: The WM Keck observatory laser guide star adaptive optics system: performance characterization. Publications of the Astronomical Society of the Pacific **118**(840), 310–318 (2006)
17. Darestani, M.Z., Heckel, R.: Accelerated MRI with un-trained neural networks. IEEE Transactions on Computational Imaging **7**, 724–733 (2021)
18. Davies, R., Kasper, M.: Adaptive optics for astronomy. Annual Review of Astronomy and Astrophysics **50**(1), 305–351 (2012)
19. De Groot, P.: Phase shifting interferometry. In: Optical Measurement of Surface Topography, pp. 167–186. Springer (2011)

20. De Groot, P.J.: Vibration in phase-shifting interferometry. Journal of the Optical Society of America A **12**(2), 354–365 (1995)
21. Falldorf, C., Agour, M., v. Kopylow, C., Bergmann, R.B.: Phase retrieval by means of a spatial light modulator in the Fourier domain of an imaging system. Applied Optics **49**(10), 1826–1830 (2010)
22. Fienup, J.R.: Phase retrieval algorithms: a comparison. Applied Optics **21**(15), 2758–2769 (1982)
23. Gandelsman, Y., Shocher, A., Irani, M.: Double-dip: unsupervised image decomposition via coupled deep-image-priors. In: IEEE Conf. Comput. Vis. Pattern Recog. (2019)
24. Gerchberg, R.W.: A practical algorithm for the determination of the phase from image and diffraction plane pictures. Optik **35**(2), 237–246 (1972)
25. Glückstad, J., Mogensen, P.C.: Optimal phase contrast in common-path interferometry. Applied Optics **40**(2), 268–282 (2001)
26. Goldstein, R.M., Zebker, H.A., Werner, C.L.: Satellite radar interferometry: Two-dimensional phase unwrapping. Radio Science **23**(4), 713–720 (1988)
27. Goodman, J.W.: Introduction to Fourier Optics. Roberts & Company (2005)
28. Hampson, K.M., Turcotte, R., Miller, D.T., Kurokawa, K., Males, J.R., Ji, N., Booth, M.J.: Adaptive optics for high-resolution imaging. Nature Reviews Methods Primers **1**(1), 68 (2021)
29. Hariharan, P.: Basics of interferometry. Elsevier (2010)
30. Hariharan, P., Oreb, B.F., Eiju, T.: Digital phase-shifting interferometry: a simple error-compensating phase calculation algorithm. Applied Optics **26**(13), 2504–2506 (1987)
31. Herráez, M.A., Burton, D.R., Lalor, M.J., Gdeisat, M.A.: Fast two-dimensional phase-unwrapping algorithm based on sorting by reliability following a noncontinuous path. Applied Optics **41**(35), 7437–7444 (2002)
32. Huang, Z., Cao, L.: Quantitative phase imaging based on holography: trends and new perspectives. Light: Science & Applications **13**(1), 145 (2024)
33. Hyder, R., Cai, Z., Asif, M.S.: Solving phase retrieval with a learned reference. In: Eur. Conf. Comput. Vis. (2020)
34. Işil, Ç., Oktem, F.S.: Deep plug-and-play HIO approach for phase retrieval. Applied Optics **64**(5), A84–A94 (2025)
35. Ji, N.: Adaptive optical fluorescence microscopy. Nature Methods **14**(4), 374–380 (2017)
36. Kamilov, U.S., Mansour, H., Wohlberg, B.: A plug-and-play priors approach for solving nonlinear imaging inverse problems. IEEE Signal Processing Letters **24**(12), 1872–1876 (2017)
37. Katkovnik, V., Shevkunov, I., Petrov, N.V., Egiazarian, K.: Computational super-resolution phase retrieval from multiple phase-coded diffraction patterns: simulation study and experiments. Optica **4**(7), 786–794 (2017)
38. Kaya, M.O., Oktem, F.S.: DDRM-PR: Fourier phase retrieval using denoising diffusion restoration models. Applied Optics **64**(5), A95–A105 (2025)
39. Kohler, C., Zhang, F., Osten, W.: Characterization of a spatial light modulator and its application in phase retrieval. Applied Optics **48**(20), 4003–4008 (2009)
40. Lai, G., Yatagai, T.: Generalized phase-shifting interferometry. Journal of the Optical Society of America A **8**(5), 822–827 (1991)
41. Malacara, D.: Optical shop testing. John Wiley & Sons (2007)
42. Medecki, H., Tejnil, E., Goldberg, K., Bokor, J.: Phase-shifting point diffraction interferometer. Optics Letters **21**(19), 1526–1528 (1996)

43. Metzler, C., Schniter, P., Veeraraghavan, A., Baraniuk, R.: prDeep: Robust phase retrieval with a flexible deep network. In: Int. Conf. Mach. Learn. (2018)
44. Netrapalli, P., Jain, P., Sanghavi, S.: Phase retrieval using alternating minimization. In: Adv. Neural Inform. Process. Syst. (2013)
45. Oti, J.E., Canales, V.F., Cagigal, M.P.: Analysis of the signal-to-noise ratio in the optical differentiation wavefront sensor. Optics Express **11**(21), 2783–2790 (2003)
46. Park, Y., Depeursinge, C., Popescu, G.: Quantitative phase imaging in biomedicine. Nature Photonics **12**(10), 578–589 (2018)
47. Platt, B.C., Shack, R.: History and principles of Shack-Hartmann wavefront sensing. Journal of Refractive Surgery **17**(5), S573–S577 (2001)
48. Ragazzoni, R.: Pupil plane wavefront sensing with an oscillating prism. Journal of Modern Optics **43**(2), 289–293 (1996)
49. Rhoadarmer, T.A.: Development of a self-referencing interferometer wavefront sensor. In: Advanced Wavefront Control: Methods, Devices, and Applications II (2004)
50. Rivenson, Y., Zhang, Y., Günaydın, H., Teng, D., Ozcan, A.: Phase recovery and holographic image reconstruction using deep learning in neural networks. Light: Science & Applications **7**(2), 17141–17141 (2018)
51. Roddier, F.: Adaptive optics in astronomy. Cambridge University Press (1999)
52. Rodenburg, J.M.: Ptychography and related diffractive imaging methods. Advances in Imaging and Electron Physics **150**, 87–184 (2008)
53. Romano, Y., Elad, M., Milanfar, P.: The little engine that could: Regularization by denoising (RED). SIAM Journal on Imaging Sciences **10**(4), 1804–1844 (2017)
54. Schnars, U., Jüptner, W.P.: Digital recording and numerical reconstruction of holograms. Measurement Science and Technology **13**(9), R85–R101 (2002)
55. Servin, M., Cywiak, M., Davila, A.: Lateral shearing interferometry: theoretical limits with practical consequences. Optics Express **15**(26), 17805–17818 (2007)
56. Shoushtari, S., Liu, J., Kamilov, U.S.: Diffusion models for phase retrieval in computational imaging. In: 2023 57th Asilomar Conference on Signals, Systems, and Computers (2023)
57. Smartt, R., Steel, W.: Theory and application of point-diffraction interferometers. Japanese Journal of Applied Physics **14**(S1), 351 (1975)
58. Tyson, R.K., Frazier, B.W.: Principles of adaptive optics. CRC press (2022)
59. Ulyanov, D., Vedaldi, A., Lempitsky, V.: Deep image prior. In: IEEE Conf. Comput. Vis. Pattern Recog. (2018)
60. Vakhtin, A.B., Kane, D.J., Wood, W.R., Peterson, K.A.: Common-path interferometer for frequency-domain optical coherence tomography. Applied Optics **42**(34), 6953–6958 (2003)
61. Velghe, S., Primot, J., Guérineau, N., Haïdar, R., Demoustier, S., Cohen, M., Wattellier, B.: Advanced wave-front sensing by quadri-wave lateral shearing interferometry. In: Interferometry XIII: Techniques and Analysis (2006)
62. Vellekoop, I.M., Mosk, A.P.: Focusing coherent light through opaque strongly scattering media. Optics Letters **32**(16), 2309–2311 (2007)
63. Vérinaud, C., Le Louarn, M., Korkiakoski, V., Carbillet, M.: Adaptive optics for high-contrast imaging: pyramid sensor versus spatially filtered Shack-Hartmann sensor. Monthly Notices of the Royal Astronomical Society: Letters **357**(1), L26–L30 (2005)
64. Wang, K., Song, L., Wang, C., Ren, Z., Zhao, G., Dou, J., Di, J., Barbastathis, G., Zhou, R., Zhao, J., et al.: On the use of deep learning for phase recovery. Light: Science & Applications **13**(1), 4 (2024)
65. Wolf, E.: Three-dimensional structure determination of semi-transparent objects from holographic data. Optics Communications **1**(4), 153–156 (1969)

66. Wu, Y., Sharma, M.K., Veeraraghavan, A.: WISH: Wavefront imaging sensor with high resolution. Light: Science & Applications **8**(1), 44 (2019)
67. Wyant, J.C.: Dynamic interferometry. Optics and Photonics News **14**(4), 36–41 (2003)
68. Yoshizawa, T.: Handbook of optical metrology: Principles and Applications. CRC press (2009)
69. Zhang, F., Pedrini, G., Osten, W.: Phase retrieval of arbitrary complex-valued fields through aperture-plane modulation. Physical Review A **75**(4), 043805 (2007)
70. Zhang, K., Li, Y., Zuo, W., Zhang, L., Van Gool, L., Timofte, R.: Plug-and-play image restoration with deep denoiser prior. IEEE Trans. Pattern Anal. Mach. Intell. **44**(10), 6360–6376 (2021)
71. Zheng, G., Horstmeyer, R., Yang, C.: Wide-field, high-resolution Fourier ptychographic microscopy. Nature Photonics **7**(9), 739–745 (2013)
72. Zuo, C., Qian, J., Feng, S., Yin, W., Li, Y., Fan, P., Han, J., Qian, K., Chen, Q.: Deep learning in optical metrology: a review. Light: Science & Applications **11**(1), 39 (2022)